

# Estimating spatial patterns of air temperature at building-resolving spatial resolution in Seoul, Korea

Chaeyeon Yi,<sup>a</sup> Kyu Rang Kim,<sup>b\*</sup> Seung Man An,<sup>c</sup> Young-Jean Choi,<sup>a</sup> Achim Holtmann,<sup>d</sup> Britta Jänicke,<sup>d</sup> Ute Fehrenbach<sup>d</sup> and Dieter Scherer<sup>d</sup>

<sup>a</sup> Weather Information Service Engine (WISE) Project, KMA, Korea

<sup>b</sup> Applied Meteorology Research Lab, National Institute of Meteorological Research, Jeju, Korea

<sup>c</sup> Department of Landscape Architecture, Sungkyunkwan University, Korea,

<sup>d</sup> Department of Ecology, Technische Universität Berlin, Germany

**ABSTRACT:** The thermal environment in urban areas is substantially influenced by local surface properties and their modification through human activities. The effects of urban climate on human health are one of the motivations for the development of various urban climate analysis tools. Climate Analysis Seoul (CAS) is a tool that incorporates a meso-scale atmospheric model and conceptual geographic information system (GIS)-based models to provide gridded air temperature deviations based on high-resolution land cover information. The CAS output was evaluated using air temperatures observed at 18 automatic weather stations (AWS) located in the detail region (DR) Eunpyeong. Correlation analyses were performed to reveal the influence of different land cover characteristics and CAS output variables on measured air temperature deviations. Based on the results of the correlation analyses in the study region (SR) Seoul, a regression model (total air temperature distribution, TD') was developed. It predicts spatially distributed air temperatures based on morphological parameters and an observed reference temperature. Using the TD' model, maps of daily maximum air temperatures were produced for the entire area of Seoul with a horizontal resolution of 25 m, and of 5 m for the DR, the latter allows to assess the impacts of different building and vegetation structures on air temperature by resolving buildings. The TD' model was evaluated using measurements at eight AWS. The TD' model slightly overestimated daily maximum air temperatures in 2007 and 2011, but performed better for 2011, mainly because land cover data represent the final state of the urban development. The TD' model appears to be a suitable tool for estimating air temperature distributions at building-resolving resolutions. It can be used to assess changes in the thermal environment and heat-related hazards through urban development plans already ahead of their realization.

KEY WORDS urban climate analysis; urban planning; urban heat island; urban multi-scale temperature distribution

Received 7 May 2014; Revised 31 March 2015; Accepted 5 April 2015

## 1. Introduction

Climate changes in urban areas are driven mainly by human activities including urbanization – building construction, vegetation removal, and anthropogenic heat production. Human-induced urban development involves changes in topography and landscape in many cases. In addition, it changes temperature, humidity, and wind through the changes of physical properties of the land cover during urban development (Oke, 1982; Schaer and Jendritzky, 2004; Stott *et al.*, 2004).

Atmospheric weather conditions can be divided into four classes: macro- ( $10^5$ – $10^8$  m), meso- ( $10^4$ – $2 \times 10^5$  m), local- ( $10^2$ – $5 \times 10^4$  m), and micro- ( $10^{-2}$ – $10^3$  m) scale based on the spatial coverage and spatiotemporal resolution (Oke, 1987). Local climate conditions are affected by interactions between the meso- and micro-scale weather conditions. They are results of thermal and mechanical

characteristics of local area. Characteristic components of spatial structure include density, height, area, layout, and surface properties of buildings and vegetation as well as the topography. Near-surface temperature is mainly influenced by the land cover, such as vegetation and buildings, and is highly variable with respect to time and meteorological conditions.

There are several methods available for urban climate analysis (Grimmond *et al.*, 2010): model-based analysis using models with various resolutions as, for example, computational fluid dynamics (CFD) models for wind conditions (Cui *et al.*, 2004; Baik *et al.*, 2009; Ryu *et al.*, 2011; Ryu and Baik, 2012); observation-based analysis for detailed mapping of climatic conditions considering lapse rate over terrain, urban effect, cold air drainage, and solar radiation (Chung *et al.*, 2006, 2009; Yun, 2007, 2010; Seo *et al.*, 2008); and statistical analysis on spatiotemporal structure of urban heat islands (Kim and Baik, 2005; Chow and Roth, 2006; Roth, 2007). In recent studies, resolutions of models for local climate analysis have generally increased. As the models are provided with input data of higher resolution, the resulting output also shows

\*Correspondence to: K. R. Kim, Applied Meteorology Research Lab, National Institute of Meteorological Research, 33 Seohobuk-ro, Seogwipo-si, Jeju-do 63568, Rep. of Korea. E-mail: krk9@kma.go.kr

variations over space and time in more detail. However, the observational networks that are required to optimize and evaluate these models need to be of higher spatial density as well (Lengfeld and Ament, 2012).

The population of Seoul is larger than 10 million and it is the world's fourth most populous city (UBIN, 2010; ubin.krihs.re.kr, original source: www.un.org). During the recent years, the Urban Heat Island (UHI) was recognized as one of the detrimental side effects of urbanization, and the city government started a policy to reduce the UHI through urban planning (e.g. SMG, 2009). The air temperature increase rate in Seoul during the last century was 1.4 times as high as the average increase rate of Korea, and 3.3 times as high than the global average increase rate (NIMR, 2009). In Seoul, a number of urban automatic weather stations (AWSs) were installed on roof-tops. Their average spacing is about 5.5 km, which is not adequate to capture local variations of urban features. Meso-scale analysis revealed a distinctive urban heat island in the Seoul metropolitan area (Bhang and Park, 2009). Local land cover within a 200 m radius from each observational site, as well as the distance from the centre of the city, affected temperature difference between the AWSs (Kim *et al.*, 2013; Yi *et al.*, 2014). Therefore, we need to investigate the details of the local urban features to determine their thermal and mechanical characteristics.

The conventional weather observational network in Seoul has two shortcomings for climate analysis: (1) The high installation height does not detect surface weather conditions by which people are affected, and (2) the low horizontal resolution does not represent the high variability of land cover. To overcome such shortcomings, satellite images were incorporated in the analysis of surface temperature (Bhang and Park, 2009) and model-based analyses such as Climate Analysis Seoul (CAS) were developed to analyse urban land cover data to estimate the local impact of buildings and vegetation on the thermal environment during day and night (Yi *et al.*, 2010, 2011a, 2012a).

In order to analyse the climate of complex urban areas, it is essential to integrate two different levels of analyses: meso-scale and micro-scale analyses. Meso-scale analysis can be performed dynamically by numerical weather models, whereas micro-scale analysis can be driven by static geographic information system (GIS) analysis of land cover as well as by models using building-resolving large eddy simulation (LES) and CFD models. GIS input data may easily be updated as needed to assess scenarios of urban development over small areas by GIS methods. The analyses of both meso- and micro-scale can support each other by providing a dynamic analysis of an event such as a heat wave and building-resolving analysis for development plans (Yi *et al.*, 2012b).

In this study, the methods involved in developing a hybrid climate analysis model of two different spatial scales (Kim *et al.*, 2014) will be further explained in detail. The individual component variables of CAS are compared to observed temperatures in Seoul. Finally, a flexible model scheme is developed to estimate the temperature

distribution at a spatial resolution of 5 m and tested in a new-town development in Seoul. The urban canopy properties of building height, volume, and coverage were utilized to quantify the unresolved temperature variation by the meso-scale models. The new scheme will provide a clue to solve the problem of heat stress of pedestrians at the street level ( $\sim 1.5$  m), which is different from that at typical meso-scale analysis level ( $\sim 10$  m).

## 2. Materials and methods

### 2.1. Study area and observational data

The CAS workbench was developed to determine the influence of buildings and vegetation areas on near-surface air temperature and wind conditions within the Seoul metropolitan area (Yi *et al.*, 2010). CAS uses three different nested domains for the meso-scale model shown in Figure 1. Seoul and the surrounding area were selected as a study region (SR,  $50 \times 40$  km), and a small area, Eunpyeong, in the SR was selected as a detail region (DR,  $8 \times 6$  km) for further investigation. The SR is nested inside the model region (MR,  $200 \times 200$  km). The MR covers the north-western part of the Korean peninsula (Figure 1). The DR includes a new-town area, which underwent a series of construction periods from 2007 to 2010.

In the SR, there were 51 weather stations including the Seoul weather station (SWS, Korea climate station #47108). SWS was the sole synoptic station in the region, whereas the others were urban AWS (Figure 1). Most of the urban AWSs were installed on top of 2–4 story public buildings and measured air temperature at 1.5 m above roof top and at about 10 m above ground. A few AWSs had relative humidity sensors. The SWS was selected as the reference because it has a long record of data – longer than 100 years – and it is the reference site of Seoul in the Korea standard climate change scenarios. All weather stations are installed and maintained by the Korea Meteorological Administration (KMA). Real-time weather observations along with some of their meta-data can be accessed through the official web pages ([http://www.kma.go.kr/weather/observation/aws\\_table\\_popup.jsp](http://www.kma.go.kr/weather/observation/aws_table_popup.jsp) in Korean).

In the DR, 18 air temperature and humidity stations were installed at 1.5 m above ground. Among them, eight sites (P1, P2, P4–P9) were operated since March 2007. The other 10 sites (P10–P19) were installed inside the new-town area in September 2010 when the construction was almost finished (Figure 2). The 'P' sensors were installed inside the urban canopy to monitor the pedestrians' environment. They were suitable for capturing the micro-climate effects by nearby buildings and vegetation. However, this micro-scale deviation could predominate over the meso-scale deviation. For the meso-scale weather conditions, higher measurement height such as with the urban AWSs, which were installed at about 10 m above ground, is advantageous. The 10 m measurement height is the same as in the meso-scale model variable MD (Section 2.2.2.1). The impacts of the measurement height

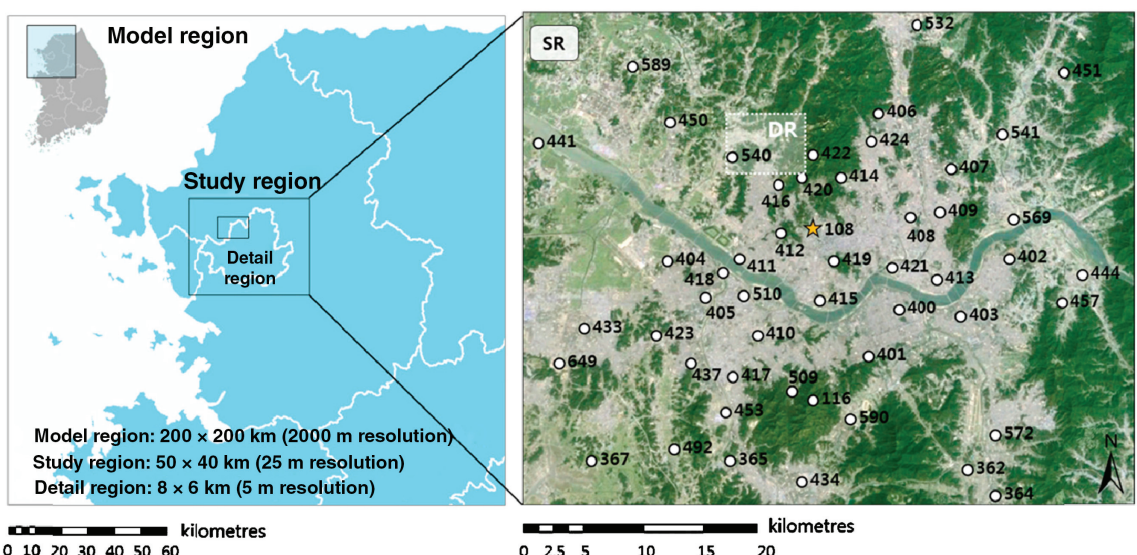


Figure 1. Nested domains for Climate Analysis Seoul (CAS): model region (MR), study region (SR) Seoul, and detail region (DR) Eunpyeong (left). Automatic weather stations (AWS) are marked by numbers in the SR (right). The average sensor height of the AWSs was 1.5 m above roof top, and the data were collected every minute. The reference Seoul weather station (SWS) is marked by a star. All weather stations in SR are official sites of KMA.

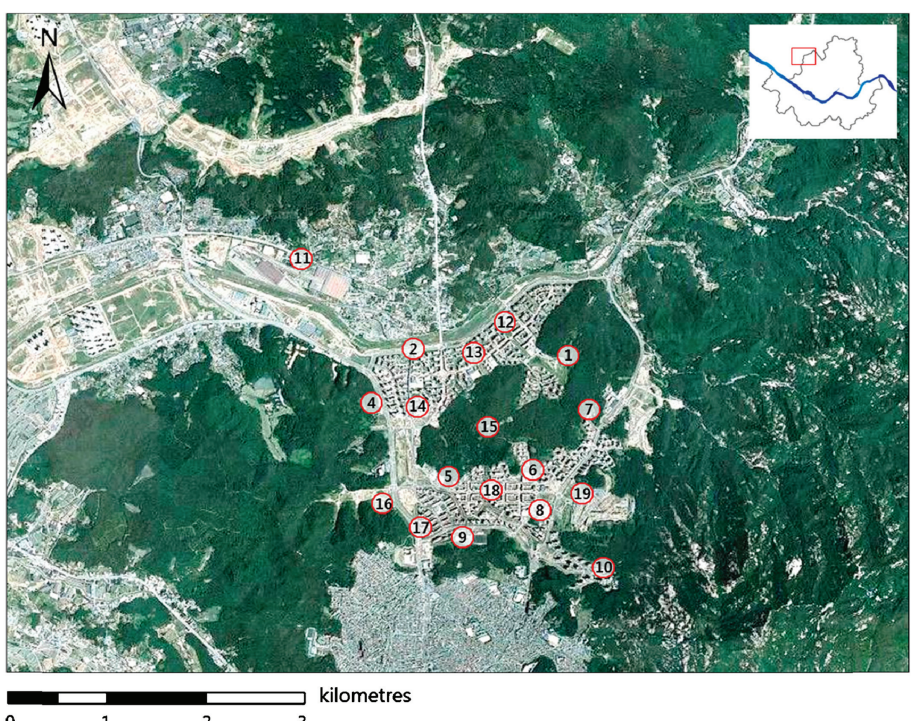


Figure 2. Observational network of 'P' sites in the DR, which experienced a new-town development since 2007. The weather stations are equipped with air temperature and relative humidity sensors at a height of 1.5 m. All 'P' sites except P11 are installed inside the new-town area.

are examined in the multi-scale temperature comparison (Section 3.1.2).

GIS data on buildings and vegetation were utilized in the development of the CAS workbench. Airborne LiDAR data (ALS50, 2009; density: 2.5 points/m<sup>-2</sup>) from the National Geographic Information Institute and high-resolution optical satellite images (KOMPSAT-2, 2009; resolution: 4 m) from the Korea Aerospace Research Institute were assimilated in CAS to produce digital terrain

and surface models, as well as land cover gridded datasets for the SR and the DR at spatial resolutions of 25 and 5 m, respectively (Yi *et al.*, 2011a, 2012a). Fractional coverage of five land cover classes (BS, built-up surfaces; US, unvegetated surfaces including bare soil and impermeable pavement; VS, vegetated surfaces; TV, tall vegetation; and WS, water surfaces) were determined based on the methods for areal types by Scherer *et al.* (1999) and GIS input data (Figures 3 and 4). Land cover

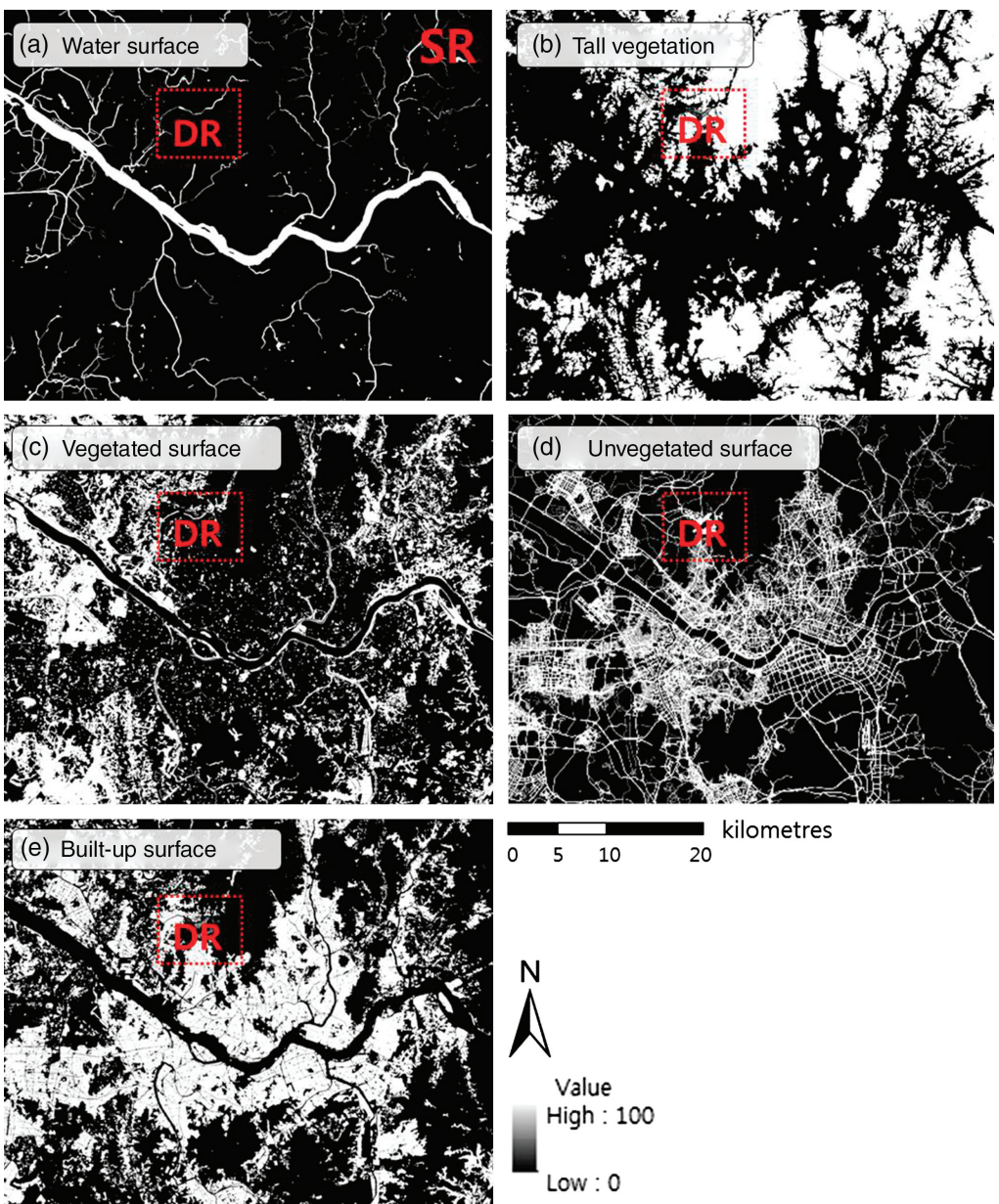


Figure 3. Fractional coverage (%) maps from CAS in the SR for five land cover classes (WS, TV, VS, US, and BS), which are determined by the LiDAR data and satellite images and have a horizontal resolution of 25 m [source: LiDAR data – National Geographic Information Institute (2009), satellite image – Korea Aerospace Research Institute (2009)].

features with height > 2 m such as TV and BS were determined by LiDAR data. The other features – VS, WS, and US – were determined using the satellite images.

The Shuttle Radar Topography Mission digital topographic data (SRTM, 2000; resolution: 90 m) and Moderate Resolution Imaging Spectrometer land cover data (MODIS, 2004; resolution 1 km) from NASA were utilized for the MR at a spatial resolution of 1 km (Yi *et al.*, 2011a, 2011b).

## 2.2. CAS workbench and component models

### 2.2.1. CAS workbench

CAS is a modelling workbench for the spatial characterization of local urban climate. It incorporates a suite

of numerical models and diagnostic tools for simulating, analysing, and visualizing meso- and local-scale climate controls and weather phenomena, and their influence on urban climate. It provides a consistent workflow of data management, processing, and visualization (Kim *et al.*, 2014).

The rule-based climate analysis and evaluation tools in CAS were originally developed to produce urban climate analysis and planning support maps for mid-latitude European cities such as Basel, Switzerland, and the Canton of Solothurn, Switzerland (Scherer *et al.*, 1999). They were improved through the processes of regional applications at different locations such as the Southern upper Rhine region in Germany (REKLISO: Parlow *et al.*, 2006), Seoul, Korea [Climate Analysis Maps for Planning Usage

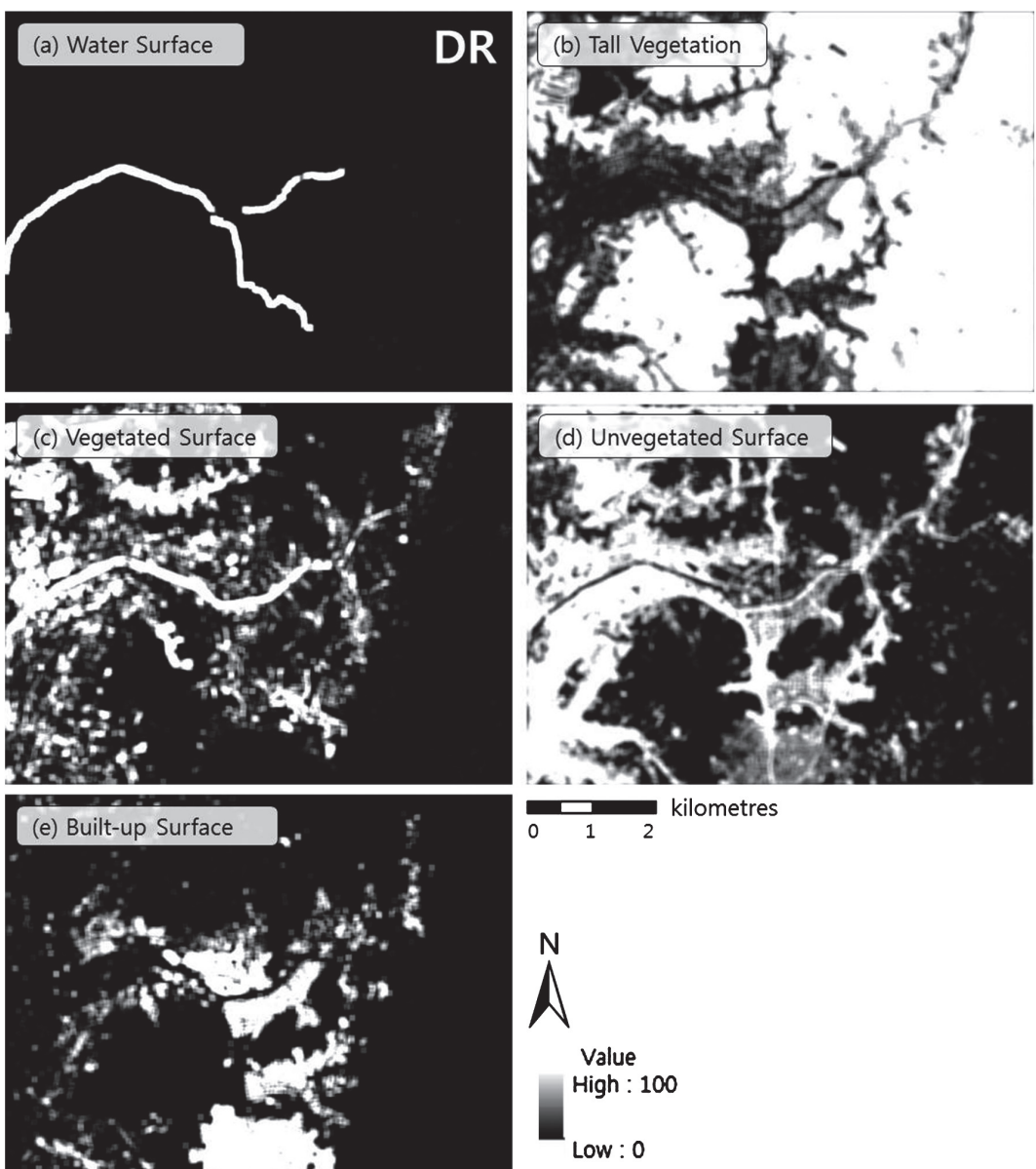


Figure 4. Fractional coverage (%) gridded datasets from CAS in the DR for five land cover classes (WS, TV, VS, US, and BS), which are determined by the LiDAR data and satellite images. It has a horizontal resolution of 5 m [source: LiDAR data – National Geographic Information Institute (2009), satellite images – Korea Aerospace Research Institute (2009)].

in Seoul (CAMPUS): Eum, 2008], and Zurich, Switzerland (KLAZ: Parlow *et al.*, 2010).

#### 2.2.2. Temperature analysis models

The assumption of CAS is that the two different spatial scales in the process of urban climatic modifications are independent of each other. The total air temperature deviation (TD) is the sum of the meso-scale air temperature deviation (MD) and the local-scale air temperature deviation (LD) by assumption. MD, LD, and TD are computed by the CAS workflow as spatially changing variables to represent spatial temperature deviation rather than being meteorological variables (Yi *et al.*, 2012a).

##### 2.2.2.1. Meso-scale temperature deviation (MD):

For MD, the prognostic three-dimensional Eulerian

model MetPhoMod (METeorology and PHOtochemistry MODel) was incorporated. It was specifically designed for photochemistry simulations in complex terrain, and an evaluation found that the model delivers accurate results according to the measurements of air temperature at 500 m resolution (Perego, 1999).

Model runs were performed in the MR, SR, and DR using one-way nesting of the three domains (Figure 1). Table 1 presents the model set-up. The  $k$ - $\varepsilon$  turbulence closure scheme of MetPhoMod applied in this study does not allow for running simulations using grid spacing values less than 100 m, as well as for vertical layers that are closer to each other than 5 m. It should be noted that the MetPhoMod simulations might have underestimated temperature variation by the parameterization of turbulent heat flux densities, which is a general requirement and

Table 1. Model configuration and physics used in the MetPhoMod simulations.

Category	Value(s)
Model domain	MR: Cartesian grid of $100 \times 100$ grid points, 2000 m grid spacing SR: Cartesian grid of $100 \times 80$ grid points, 500 m grid spacing DR: Cartesian grid of $80 \times 60$ grid points, 100 m grid spacing
Vertical layers	60 vertical layers between 10 and 6300 m a.s.l.
Surface properties	Gridded data of surface height, albedo, emissivity, aerodynamic roughness length, volumetric heat capacity, thermal diffusivity, surface temperature and time-constant temperature at 1 m depth
Model physics	Air pressure non-hydrostatic, $k$ - $\epsilon$ turbulence closure, full radiation and soil physics, wind advection, no clouds, no border dampening, no spatial filtering
Time period	Start: 21 June 0600 KST, end: 22 June 1800 KST; first 12 h discarded to remove spin-up effects
Time interval	Regular time steps of 10 s; adaptive time steps down to 1 s
Nesting	One-way nesting MR $\rightarrow$ SR $\rightarrow$ DR; forcing data from parent domains applied every 15 min
Initial conditions	No wind, i.e. $u = v = w = 0 \text{ m s}^{-1}$ Vertically constant virtual potential temperature = $20^\circ\text{C}$ Vertically constant mixing ratio = $0.4 \text{ g kg}^{-1}$ Surface temperature provided as spatially distributed values
Lateral boundary conditions (MR)	No wind, i.e. $u = v = w = 0 \text{ m s}^{-1}$ Virtual potential temperature of each vertical layer is set to layer mean value
Output variables	Data storage every 30 min: 3-dim: air pressure-, wind-, and air temperature fields 2-dim: wind-, and air temperature fields at 10 m above the momentum-absorbing surface 2-dim: full set of energy balance components (surface fluxes) and boundary layer variables

source of errors of any Reynolds-Averaged Navier Stokes (RANS) model. This problem is generally found in urban areas where horizontal homogeneity is not given, even for coarse model grids that have grid spacing values larger than 500 m. It should also be regarded that MetPhoMod resolves only meso-scale processes leading to spatially varying air temperatures, even for the high-resolution grid (grid spacing 100 m) used for the DR. The underestimated heat flux and temperature deviation can be compensated by introducing building-resolving explicit temperature deviations by GIS analysis.

The MR simulation only serves to define physically consistent lateral atmospheric boundary conditions for the SR. An ideal condition of a clear summer day with no wind initialized was simulated (Table 1). Air temperature values at a height of 10 m above ground level were obtained from the MetPhoMod simulations for the SR and DR and temporally averaged over 2000–0600 KST (UTC+9) to obtain nocturnal mean values for each grid point. Ten metre height is assumed to be within the buildings' canopy layer. The spatial average of the nocturnal mean air temperature in the SR served as the reference temperature, which was subtracted from the nocturnal mean value at each grid point to yield spatially varying values for the MD (Yi *et al.*, 2011a). MD was estimated for 10 m above ground level at 500 m horizontal resolution for SR (Figure 5(a)) and 100 m horizontal resolution for DR (Figure 6(a)).

**2.2.2.2. Local-scale temperature deviation (LD):** A GIS-based empirical-statistical model was developed to compute the LD. The GIS-based model accounts for three different local-scale processes controlling the LD: release of heat from the surface to the atmosphere (and vice

versa) by sensible heat flux, dispersal of heat by turbulent mixing, and cooling of the air due to cold-air production on surface level.

Following a study by Christen and Vogt (2004), rural, suburban and urban sites show different mean values of the dimensionless ratio of sensible heat flux density and net radiation during the nighttime, depending on the complete surface aspect ratio ( $f_{\text{CSAR}}$ ).  $f_{\text{CSAR}}$  is 1 for areas without buildings and larger than 1 for built-up areas, because their walls also contribute to the total surface. CAS estimated gridded  $f_{\text{CSAR}}$  values from the data on fractional coverage of built-up surfaces  $f_{\text{BS}}$  and the mean height of buildings  $h_{\text{B}}$  with Equation (1)

$$f_{\text{CSAR}} = 1 + 4 \cdot \sqrt{f_{\text{BS}}} \cdot \frac{h_{\text{B}}}{d_s} \quad (1)$$

for an idealized building geometry with a single building per grid cell with four walls of equal size and a flat roof. Fractional coverage  $f_{\text{BS}}$  and fractional coverage for other land cover types, as well as  $f_{\text{CSAR}}$  values, were computed in CAS for grid cells of 1 ha size centred on each grid point. Therefore, the grid cells have an extent  $d_s$  (100 m), which is much larger than the grid spacing of land cover data in the DR (5 m) to consider local-scale effects stemming from land cover variations in adjacent areas. Increasing  $f_{\text{CSAR}}$  values are assumed to lead to higher nocturnal sensible heat flux densities away from the building surfaces (Christen and Vogt, 2004) and subsequent warming of high density urban quarters, which was estimated as the following Equation (2):

$$dT_{\text{SHF}} = c_{\text{SHF}} \cdot (f_{\text{CSAR}} - 1) \quad (2)$$

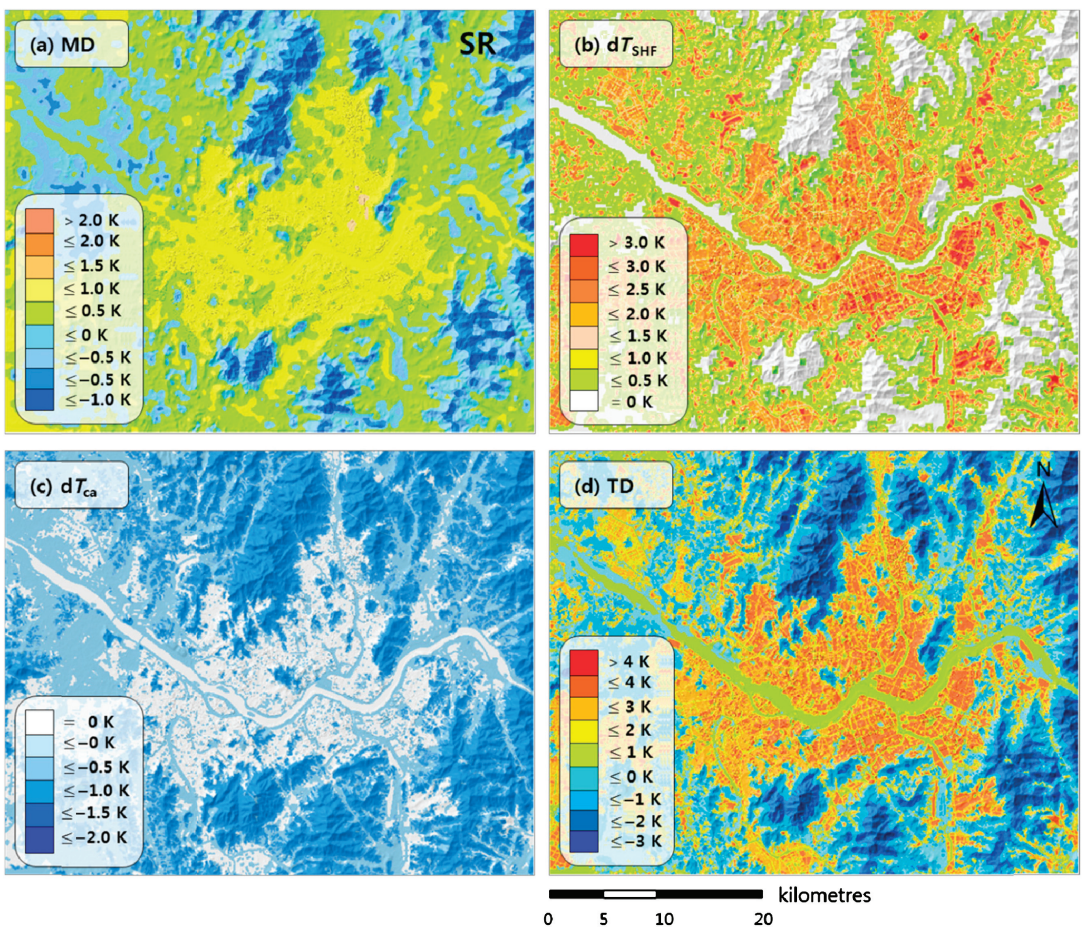


Figure 5. (a) Meso-scale temperature deviation (MD), (b) nocturnal sensible heat release by buildings ( $dT_{SHF}$ ), (c) decrease in air temperature by local cooling ( $dT_{ca}$ ), and (d) total temperature deviation (TD) in the SR. Hill shading indicates the mountainous topography. MD (a) is the average night time (2000–0600) air temperature deviation of an ideal case of 21–22 June.  $dT_{SHF}$  (b) and  $dT_{ca}$  (c) are computed by empirical-statistical models based on the fractional coverage of land cover classes.

where  $dT_{SHF}$  is the local-scale increase in air temperature due to nocturnal sensible heat released by the built-up surface into the atmosphere, and  $c_{SHF}$  is an empirical coefficient, which was set to a value of 2 K per unit increase in  $f_{CSAR}$ . Equation (2) ensures that air temperature in areas without buildings ( $f_{CSAR} = 1$ ) remains unchanged. It should be noted that the choice of the value of  $c_{SHF}$  has to consider that the warming of the air by nocturnal release of sensible heat in built-up areas is partly already computed by the MetPhoMod simulations, thus  $dT_{SHF}$  only represents the unresolved local-scale contribution to nocturnal UHI formation. The validity of the selected value of  $c_{SHF}$  can be found in the comparison of the actual observations described in Sections 2.3 and 3.1. The resolved and unresolved heat releases were actually determined by the observation described in Section 3.2.1.

Dispersion of heat by turbulent mixing smoothes the effect of sensible heat release such that the actual increase in air temperature  $dT'_{SHF}$  is smaller than  $dT_{SHF}$  for a point source, while adjacent areas will experience a slight increase in air temperatures. This effect is considered in CAS by convolving the gridded  $dT_{SHF}$  values with a Gaussian low pass kernel of  $20 \times 20$  grid points, i.e. over an area of 1 ha, to obtain gridded values for  $dT'_{SHF}$ .

The third effect considered in CAS for computing the LD is local cooling due to cold-air production at a rate of  $Q_{ca}$ , which is the volume of air that is cooled per unit area during 1 h. CAS computes the decrease in air temperature by local cooling  $dT_{ca}$  by

$$dT_{ca} = c_{ca} \cdot Q_{ca} = c_{ca} \cdot (f_{TV} \cdot Q_{ca,TV} + f_{VS} \cdot Q_{ca,VS}) \quad (3)$$

Here, only TV like forests or urban parks with trees, and other VS are assumed to contribute to cold-air production weighted by their fractional coverage values  $f_{TV}$  and  $f_{VS}$ , which were computed for 1-ha grid cells as for  $f_{BS}$ . Cold air production assumes that the incoming solar radiation is cut by TV and also transformed into latent heat by vegetation (TV and VS) during day. Cold air production during night assumes smaller residual heat storage of TV and VS than that of BS and US.  $Q_{ca,TV}$  is the cold-air production rate for an area solely covered by TV, while  $Q_{ca,VS}$  is the analogous value for VS. The values for  $Q_{ca,TV}$  and  $Q_{ca,VS}$  were estimated from literature references by 30 and  $15 \text{ m}^3 \text{ m}^{-2} \text{ h}^{-1}$ , respectively (see e.g. Mosimann *et al.*, 1999). The resulting  $Q_{ca}$  is multiplied by an empirical cooling factor ( $c_{ca}$ ), which was set to  $-0.05 \text{ K h m}^{-1}$  in this study.

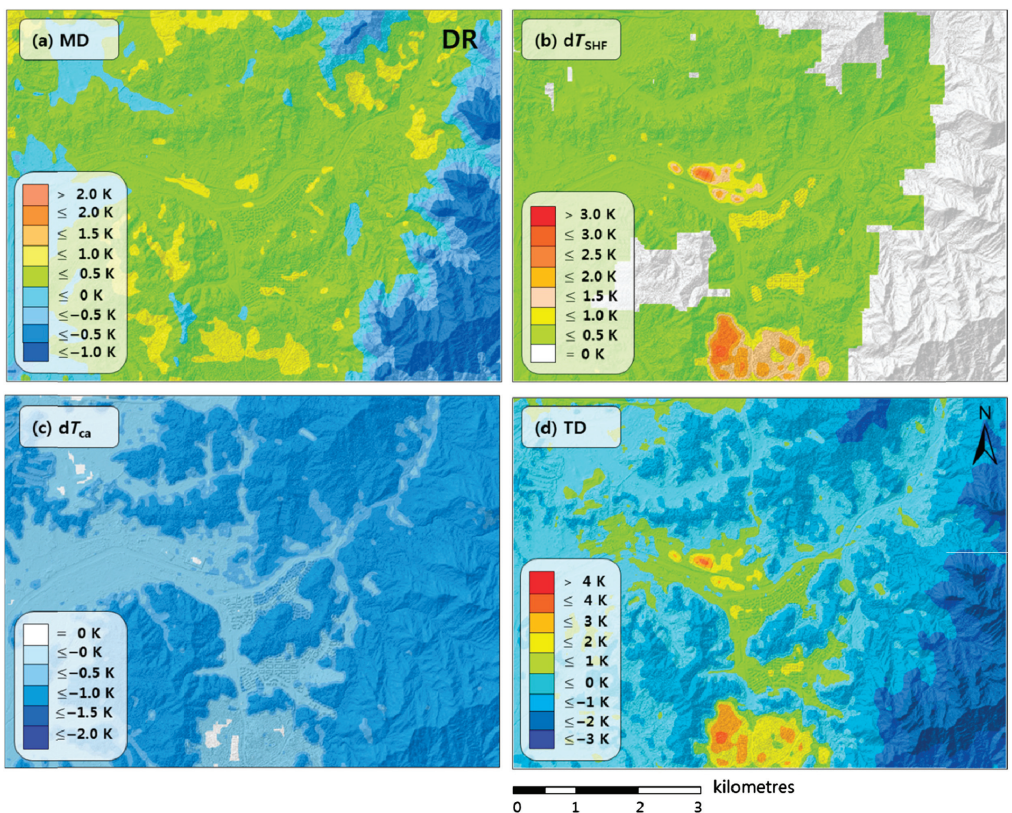


Figure 6. (a) Meso-scale temperature deviation (MD), (b) nocturnal sensible heat release by buildings ( $dT_{SHF}$ ), (c) decrease in air temperature by local cooling ( $dT_{ca}$ ), and (d) total temperature deviation (TD) in the DR. Hill shading indicates the mountainous topography. MD is the average night time (2000–0600) air temperature deviation of an ideal case of 21–22 June.  $dT_{SHF}$  and  $dT_{ca}$  are computed by empirical-statistical models based on the fractional coverage of land cover classes.

Finally, the LD was computed on the surface level as the sum of  $dT'_{SHF}$  and  $dT_{ca}$  (Equation (4)). The term  $dT_{ca}$  illustrates that the LD is mainly an indicator of local-scale nocturnal air temperature modifications because cold air production does not take place during daytime in summer. The horizontal resolution of  $dT'_{SHF}$  and  $dT_{ca}$  of LD calculation was 25 m for SR (Figure 5(b) and (c)) and 5 m for DR (Figure 6(b) and (c)).

$$LD = dT'_{SHF} + dT_{ca} \quad (4)$$

**2.2.2.3. Total temperature deviation (TD):** Total temperature deviation is calculated by

$$TD = MD + LD \quad (5)$$

for each grid point in the SR and DR. TD was positive in built-up areas but negative in suburban areas with a range of 8 K (Figures 5(d) and 6(d)).

### 2.3. Evaluation of the air temperature deviations estimated by CAS

#### 2.3.1. Comparisons between observed and estimated temperatures

The output of CAS was evaluated using the observed temperature in the DR. The nighttime (2000–0600) hourly temperatures at the 18 sites of the DR in 2011 were utilized

for the evaluation. The data with wind speeds of less than 25% of the climatic range and cloudiness of less than 30% at the SWS were selected for the comparison with the variables of CAS. The 25% level of the nighttime hourly wind speed at the SWS was calculated from the observed data at the SWS from 2002 to 2011 and determined as  $1.68 \text{ m s}^{-1}$ .

The observed temperature deviation was calculated by subtracting the mean observed air temperature at P1–P19 from each observation. The estimated temperature deviations (MD, LD, and TD) at each location (P1–P19) were extracted from the CAS output.

#### 2.3.2. Multi-scale correlation analysis between the observed temperature deviations and CAS output variables

A correlation analysis between the observed temperature deviation and different CAS output variables was performed to determine the impact of the morphological parameters on temperature distribution. The correlation results were compared among seasons, weather conditions, and domains.

Several variables were chosen from CAS and GIS analyses for the explanation of the spatial distribution of the temperature deviations. Selected variables were fractional coverages of land cover types of CAS –  $f_{BS}$  (built-up surfaces),  $f_{US}$  (all US including bare soil and asphalt or concrete pavement),  $f_{VS}$  (short vegetation), and  $f_{TV}$  (TV);

Table 2. The weather statistics in Seoul with specific weather conditions.

Class	Weather conditions	Spring	Summer	Autumn	Winter
w0	WSpd $\leq$ 25%	WSpd $\leq$ 2.10	WSpd $\leq$ 1.77	WSpd $\leq$ 1.60	WSpd $\leq$ 1.81
c0	CA $\leq$ 3	68	33	97	103
c1	3 < CA $\leq$ 7	82	69	83	85
c2	CA > 7	80	124	51	40
w1	WSpd 25–75%	2.10 < WSpd $\leq$ 3.18	1.77 < WSpd $\leq$ 2.65	1.60 < WSpd $\leq$ 2.50	1.81 < WSpd $\leq$ 2.88
c0	CA $\leq$ 3	182	74	197	211
c1	3 < CA $\leq$ 7	168	163	157	151
c2	CA > 7	111	227	98	87
w2	WSpd > 75%	WSpd > 3.18	WSpd > 2.65	WSpd > 2.50	WSpd > 2.88
c0	CA $\leq$ 3	83	19	76	124
c1	3 < CA $\leq$ 7	63	52	73	66
c2	CA > 7	83	159	78	35

Wind speed classes (WSpd: w0, w1, w2) and daily cloud amount (CA: c0, c1, c2; 0–10 scale) for the four seasons were determined based on the daily observed data at the Seoul weather station from 2002 to 2011 (total  $N = 3652$  days).

model output variables from CAS – MD, TD,  $dT_{\text{SHF}}$ , and  $dT_{\text{ca}}$ ; variables from the GIS analyses –  $h_B$  (building height),  $h_V$  (height of the TV), and  $z$  (terrain elevation).

The air temperature at the 18 sites in the DR (Figure 2) was used to represent the local temperature deviation from the reference station SWS. Wind speed and cloudiness observed at the SWS from 2002 to 2011 were utilized to determine seasonal weather class categories. A total of nine categories are defined in Table 2 based on the wind speed and cloud amount. For the correlation analysis, five weather class categories were selected (w0c0, w0c2, w1c1, w2c0, and w2c2 as underlined) to represent characteristic wind and cloudiness conditions.

The temperature deviation from the reference station was selected as the response variable to the local variations of urban features such as the layout of buildings and parks. The deviation of daily maximum temperature ( $dT_{\text{max}}$ ) at the 18 sites in the DR from March 2007 to February 2012 was calculated by subtracting the daily maximum temperature of the SWS from the observed maximum temperature. The deviation of the daily minimum temperature ( $dT_{\text{min}}$ ) was calculated in the same way as  $dT_{\text{max}}$ .  $dT_{\text{max}}$  and  $dT_{\text{min}}$  represent the daily temperature distribution of both day and night, respectively.

The correlation analysis was then extended to the SR using the observed data in and around Seoul during the same period chosen for the DR. The deviation of daily maximum and minimum temperature at the 51 AWS sites (Figure 1) from the SWS observation was calculated and correlated to the same explanatory variables as the DR.

Based on the correlation analyses for the DR and SR with the five weather classes, the characteristic weather conditions and variables were determined for further analysis of temperature distribution.

#### 2.4. Application of CAS to estimate temperature distribution (TD')

##### 2.4.1. Regression analysis in the SR to estimate temperature distribution

Because MD, LD, and thus TD, are not meteorological variables but used as relative nocturnal heat stress

indicators, an additional, empirical-statistical procedure was developed to estimate the actual spatial distribution of air temperature  $T$  (TD') for summer days with calm winds and low cloud coverage on an hourly basis. We used hourly air temperature  $T_{\text{SWS}}$  observed at the SWS and spatially distributed differences between maximum air temperature  $T_{\text{max}}$  and the maximum air temperature  $T_{\text{max,SWS}}$  at the SWS:

$$T = T_{\text{SWS}} + (T_{\text{max}} - T_{\text{max,SWS}}) + \varepsilon = T_{\text{SWS}} + dT_{\text{max}} + \varepsilon \quad (6)$$

All variables except the variables for SWS such as  $T_{\text{SWS}}$  are gridded variables ( $X[i,j]$ ) in the domains SR and DR. Differences in maximum air temperature  $dT_{\text{max}}$  are used in Equation (5) in order to minimize the residual term  $\varepsilon$  for the hottest weather conditions. The residual term  $\varepsilon$  is also the error term in the regression analysis. A stepwise regression was applied to estimate  $dT_{\text{max}}$  from a set of potential predictors. The following were selected considering the correlation analysis: air temperature deviations (MD, LD, and TD), cold-air production rate  $Q_{\text{ca}}$ , fractional coverages for the land cover classes ( $f_{\text{BS}}, f_{\text{TV}}, f_{\text{VS}}, f_{\text{US}}$ , and  $f_{\text{WS}}$ ), terrain elevation above sea level  $z$ , building height  $h_B$ , and the product of  $h_B$  and  $f_{\text{BS}}$  representing the building volume per unit area. The predictors are available as gridded data at spatial resolutions of 25 m for the SR and 5 m for the DR, respectively. Land cover was computed as the fraction of the specified class of 5 × 5 m cells in a 100 × 100 m grid. The estimated values for  $dT_{\text{max}}$  were determined by the differences between the maximum air temperatures observed at the 51 weather stations in the SR shown in Figure 1 and those at the SWS during the summer months (June, July, and August) of the years from 2007 to 2011. Only days, during which wind speed was in the lowest 25% percentile (i.e. below 1.77 m s<sup>-1</sup>) and cloud coverage in the lowest 30% percentile were taken as input in the stepwise regression to quantify the localized effects of buildings and vegetation on temperature distribution. Daily mean wind speed at the SWS from 2002 to 2011 was utilized for the categorization. In total, only eight days fulfilled the above-mentioned filter criteria of low wind and

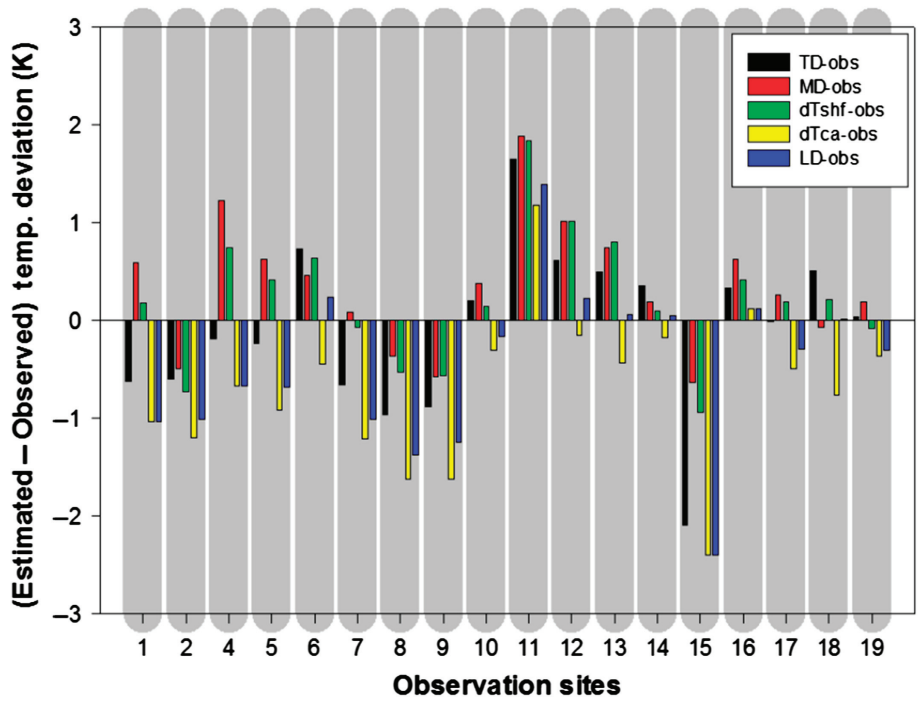


Figure 7. Differences between estimated temperature deviations (TD, MD, and LD) and observed temperature deviations in the DR. Mean differences/standard deviations were  $-0.87/0.83$ ,  $0.33/0.66$ , and  $-0.05/0.83$  K for TD, MD, and LD, respectively (see Sections 2.1 and 2.3.1 on observation and data processing).

low cloudiness. Predictor values were taken from the nearest grid points of the SR data.

#### 2.4.2. Mapping and evaluation of the detailed temperature distribution – TD'

The regression results, i.e. intercept and coefficients for those predictors finally considered in the regression model, were applied to all grid points in the SR and DR to estimate  $dT_{\max}$ , from which the hourly  $T$  distributions were finally estimated by applying Equation (6) (TD' model). Using the temperature distribution, the heat stress levels were visualized as areas with temperature exceeding certain levels of heat wave warnings.

The estimated daily maximum temperatures by the TD' model were compared with the observed maximum temperatures in the DR in the years 2007 and 2011, which represent the pre- and post-development situation, respectively. The land cover and the Digital Surface Model databases utilized in the CAS analysis represent the surface conditions after the construction.

### 3. Results and discussion

#### 3.1. Evaluation of the air temperature deviations estimated by CAS

##### 3.1.1. Comparisons between observed and estimated temperatures

The differences between the estimated and observed deviations in the DR are presented in Figure 7. The observed temperature deviations were in the range of  $-1.62$  to

$+0.95$  K and the differences between the observed and estimated deviations were about  $-2.5$  to  $+2.0$  K. In most cases, differences were smaller for the LD than for the MD or TD. The MD had the largest mean difference, which implies that the local temperature deviation could not be fully resolved by the MD so that further analysis at a higher resolution with additional information such as building and vegetation layouts was needed. In this study, the LD contributes to the TD with analysis data at higher resolution. The difference between the deviation estimated by CAS and the observed deviation reveals the need for improvements such as systematic analysis and optimization of the component variables. The contribution of the BS in the LD calculation through  $f_{CSAR}$  was fairly close to the observed temperature deviation. The observed temperature deviation at P15 was much higher than the estimated TD. This was due to the overestimated  $dT_{ca}$  by the surrounding area of TV at this site. Cold air produced by the nearby TV at P15 might have been dissipated through the downhill slope to the valley and replaced by warmer upper air, which resulted in a higher observed temperature than estimated. In the  $dT_{ca}$  calculation, topography and slope were not considered.

At P11, the temperature was overestimated near the large flat and low-rise maintenance buildings of the subway system, located in the East and West sides of the P11 (Figure 2). The big flat buildings near P11 are actually open ended ones so that the thermal impact should have been smaller compared to the other ordinary buildings. Also, it is speculated that the cold air produced during the nighttime could have stagnated around P11 due to the

topography and caused the observed lower temperature than estimated.

As described, the difference of the deviations depends on the local environment, especially on land cover. To address the variability of the local thermal impact of urban structures, it is necessary to incorporate more flexible analysis of observational data. Furthermore, local vegetation effects would be more clearly recognized if the wind direction was also considered in the analysis.

### 3.1.2. Multi-scale correlation analysis between the observed and estimated temperatures

**3.1.2.1. Correlation analysis in the DR:** The correlation analysis between the daily temperature deviations ( $dT_{\max}$  and  $dT_{\min}$ ) and CAS variables from the observational sites in the DR (Figure 2) is shown in Table 3 for four seasons. Pink denotes positive correlation coefficients, whereas blue denotes negative. Darker colours represent higher correlation coefficients.

For all seasons, the TD,  $dT_{\text{SHF}}$ ,  $dT_{\text{ca}}$ ,  $f_{\text{BS}}$ ,  $f_{\text{US}}$ , and  $f_{\text{VS}}$  of CAS had positive correlations with the temperature deviations, whereas the MD and  $f_{\text{TV}}$  of CAS had negative correlation. The correlation was stronger during summer and weaker during winter. The impact of local features, which are represented by  $f_{\text{BS}}$ ,  $f_{\text{TV}}$ ,  $dT_{\text{SHF}}$ , and  $dT_{\text{ca}}$ , was stronger with  $dT_{\max}$  than  $dT_{\min}$  although LD ( $dT_{\text{SHF}}$  and  $dT_{\text{ca}}$ ) was computed for nighttime situations.

It could be also asserted that the stronger correlation for summer was mainly related to the impact of the vegetation ( $dT_{\text{ca}}$  and  $f_{\text{TV}}$ ). The vegetation impact was stronger during daytime ( $dT_{\max}$ ) than nighttime ( $dT_{\min}$ ) although  $dT_{\text{ca}}$  was designed to explain the nighttime cold air production. The shadows casted by the leaves of tall trees in the DR may have reduced the solar radiation over the soil and building surfaces. This shadowing impact was not explicitly included in CAS and can be improved in the future.

During the winter season, positive correlations were found with  $f_{\text{US}}$  and TD whereas negative with  $f_{\text{TV}}$ . The correlation of both variables was stronger in the summer season with the low wind speed and low cloud amount condition (w0c0).

Many studies describe the air temperature deviation due to vegetation and sealed surfaces (e.g. Yu and Hien, 2006; Chow *et al.*, 2011). The results from this study emphasize the impacts of individual buildings and trees on the local climate. Meso-scale temperature deviation (MD) showed no significance or even negative correlation. This observation shows that the very local temperature distribution cannot be explained by the meso-scale temperature analysis at 100 m resolution, but it can effectively be described by the detailed variables in CAS at a 5 m resolution. The seasonal influences and cooling rates for TV due to leaf coverage difference were not considered in this study. The seasonal difference could be further explained by more detailed vegetation model explaining the forest types – deciduous or coniferous or mixed.

**3.1.2.2. Correlation analysis in the SR:** The correlation analysis between the daily temperature deviations ( $dT_{\max}$

and  $dT_{\min}$ ) and CAS variables from the observational sites in the SR is presented in Table 4 for each season. In the SR, the seasonal variation and impact of wind speed on the correlation coefficients were smaller than in the DR.  $dT_{\max}$  showed stronger correlations than  $dT_{\min}$ . This implies that the local heating during the day has a stronger impact on the local temperature distribution than the local cooling during the night.

The  $dT_{\text{SHF}}$ ,  $dT_{\text{ca}}$ , MD, TD,  $f_{\text{BS}}$ , and  $f_{\text{WS}}$  from CAS had a positive correlation, whereas  $f_{\text{TV}}$  had a negative correlation.  $h_B$  and  $h_V$  correlated positively and negatively with the temperature deviation, respectively.  $z$  was negatively correlated with the observed temperature.

In the SR, the meso-scale temperature deviation (MD) was significantly positively correlated with the observed temperature deviations (Figure 8(b) and (d)), whereas it was not significant or even negatively correlated with observations in the DR (Figure 8(a) and (c)). This is reasonable as the spacing between observation sites is much larger in the SR, and the environments of the SR sites are likely to be more different from each other than in the DR. The variation of the correlation coefficients for  $dT_{\max}$  and  $dT_{\min}$  was similar in DR (Figure 8(a) and (c)), whereas it was larger for  $dT_{\min}$  than for  $dT_{\max}$  in SR (Figure 8(b) and (d)). This suggests that the methods in this study are more reliable at the higher resolution (DR). As with  $dT_{\max}$  (Figure 8(a) and (b)), the morphological parameters ( $dT_{\text{SHF}}$  and  $dT_{\text{ca}}$ ) were able to contribute to the total temperature deviation (TD) in DR but not much in SR. Although  $dT_{\max}$  had the highest correlations coefficient with MD in SR (Figure 8(b)), the smaller overall correlation coefficient with total deviation (TD) than with MD showed the limited power in the explanation of the temperature variations by the local analysis variables ( $dT_{\text{SHF}}$  and  $dT_{\text{ca}}$ ) in the SR. Although the correlation coefficient with  $dT_{\min}$  (Figure 8(c) and (d)) was smaller than  $dT_{\max}$  (Figure 8(a) and (b)), the additive effect of the component variables ( $dT_{\text{SHF}}$ ,  $dT_{\text{ca}}$ , and MD) to the total (TD) was remarkable with  $dT_{\min}$  especially in DR. In other words, the TD in this study was the best variable that describes the minimum temperature ( $dT_{\min}$ ) in DR and SR. The current analysis methods, however, are not detailed enough to differentiate the differences between meso-scale and local-scale heating. Bottom-up approaches will be needed to understand the components of the local heating at various scales or levels such as anthropogenic heat production at building level and traffic volume at street level.

## 3.2. Application of CAS to estimate temperature distribution (TD')

### 3.2.1. Regression analysis in the SR to estimate temperature distribution

The stepwise regression analysis was conducted for the estimation of high-resolution temperature distribution (TD') from the gridded CAS data in the SR. The optimal regression model for the deviation of daily maximum

Table 3. Correlation coefficients between the CAS output variables and the temperature deviations ( $dT_{\max}$  and  $dT_{\min}$ ) from the reference station (Seoul weather station) at the 18 sites in the DR for the four seasons.

Class	Temperature	$dT_{\text{SHF}}$	$dT_{\text{ca}}$	MD	TD	$f_{\text{BS}}$	$f_{\text{US}}$	$f_{\text{VS}}$	$f_{\text{TV}}$	$h_{\text{B}}$	$h_{\text{V}}$	$z$
Spring												
w0c0	$dT_{\max}$	0.27***	0.08ns	0.13ns	0.17**	0.11ns	0.04ns	-0.07ns	-0.07ns	0.08ns	-0.36***	0.15*
	$dT_{\min}$	0.29***	0.32***	-0.24***	0.31***	0.28***	0.23***	0.05ns	-0.31***	0.20**	-0.34***	0.22***
w1c1	$dT_{\max}$	0.11***	0.10*	0.02ns	0.10***	0.00ns	0.09***	0.01ns	-0.07ns	-0.03ns	-0.23***	-0.01ns
	$dT_{\min}$	0.19***	0.18***	-0.06*	0.20***	0.20***	0.08**	0.05**	-0.18***	0.16***	-0.12***	0.17***
w2c2	$dT_{\max}$	0.04ns	0.08*	0.03ns	0.08*	0.01ns	0.09*	0.06ns	-0.09*	-0.02ns	-0.07ns	-0.13***
	$dT_{\min}$	0.18***	0.25***	-0.08ns	0.25***	0.18***	0.18***	0.08*	-0.25***	0.08*	-0.16***	-0.02ns
w0c2	$dT_{\max}$	0.14**	0.26***	-0.13**	0.23***	0.12**	0.25***	0.09*	-0.26***	0.04ns	-0.28***	-0.09ns
	$dT_{\min}$	0.13**	0.12**	0.01ns	0.14**	0.17***	0.03ns	0.04ns	-0.12**	0.15***	-0.07ns	0.04ns
w2c0	$dT_{\max}$	0.11***	0.05ns	0.06ns	0.09**	-0.03ns	0.09**	-0.02ns	-0.05ns	-0.06ns	-0.19***	-0.04ns
	$dT_{\min}$	0.18***	0.10**	0.05ns	0.15***	0.25***	-0.03ns	-0.02ns	-0.10**	0.19***	-0.00ns	0.32***
Summer												
w0c0	$dT_{\max}$	0.37***	0.63***	-0.27**	0.54***	0.29**	0.66***	0.24*	-0.62***	0.56**	-0.50**	0.27**
	$dT_{\min}$	0.21*	0.49***	-0.06ns	0.41***	0.34***	0.36***	0.35***	-0.50***	0.31**	-0.25**	-0.35***
w1c1	$dT_{\max}$	0.27***	0.54***	-0.20	0.47***	0.19***	0.53***	0.24***	-0.54***	0.35***	-0.36***	0.03ns
	$dT_{\min}$	0.17***	0.28***	0.04	0.27***	0.23***	0.16***	0.20***	-0.28***	0.22***	-0.11***	-0.11***
w2c2	$dT_{\max}$	0.24***	0.58***	-0.22***	0.49***	0.19***	0.55***	0.34***	-0.58***	0.28***	-0.32***	-0.15***
	$dT_{\min}$	0.15***	0.39***	-0.06*	0.33***	0.18***	0.32***	0.30***	-0.40***	0.21***	-0.19***	-0.24***
w0c2	$dT_{\max}$	0.27***	0.62***	-0.21***	0.53***	0.23***	0.60***	0.35***	-0.62***	0.50***	-0.29***	-0.01ns
	$dT_{\min}$	0.16***	0.39***	-0.07ns	0.34***	0.19***	0.34***	0.29***	-0.40***	0.21***	-0.16***	-0.22***
w2c0	$dT_{\max}$	0.22**	0.43***	-0.13ns	0.40***	0.11ns	0.42***	0.19**	-0.43***	0.07ns	-0.41***	-0.13ns
	$dT_{\min}$	0.28***	0.25***	0.07ns	0.31***	0.33***	0.10ns	0.02ns	-0.24***	0.25***	-0.15ns	0.06ns
Autumn												
w0c0	$dT_{\max}$	0.07ns	0.41***	-0.27***	0.30***	-0.04ns	0.50***	0.35***	-0.43***	0.07ns	-0.41***	-0.04ns
	$dT_{\min}$	0.12**	-0.03ns	0.04ns	0.03ns	0.23***	-0.16***	-0.16***	0.04ns	0.03ns	0.01ns	0.29***
w1c1	$dT_{\max}$	0.13***	0.44***	-0.22***	0.36***	0.02ns	0.49***	0.30***	-0.45***	0.11***	-0.37***	-0.08***
	$dT_{\min}$	0.15***	0.03ns	0.08***	0.09***	0.24***	-0.10***	-0.08**	-0.02ns	0.13***	0.04ns	0.27***
w2c2	$dT_{\max}$	0.16***	0.38***	-0.13***	0.33***	0.09**	0.36***	0.20***	-0.38***	0.08*	-0.27***	-0.18***
	$dT_{\min}$	0.10**	0.11**	0.04	0.13***	0.14***	0.04	0.05	-0.11**	0.09**	-0.06***	-0.01ns
w0c2	$dT_{\max}$	0.17**	0.45***	-0.22***	0.37***	0.13*	0.45***	0.27***	-0.45***	0.22***	-0.26***	-0.07ns
	$dT_{\min}$	0.09ns	0.17**	-0.08ns	0.15**	0.13*	0.11ns	0.07ns	-0.17**	0.05ns	-0.10ns	-0.01ns
w2c0	$dT_{\max}$	0.13***	0.44***	-0.11*	0.37***	0.03ns	0.45***	0.32***	-0.45***	0.16***	-0.35***	-0.16***
	$dT_{\min}$	0.22***	0.18***	0.09*	0.23***	0.34***	0.00ns	0.02ns	-0.18***	0.16***	-0.09**	0.14***
Winter												
w0c0	$dT_{\max}$	0.08ns	0.29***	-0.07ns	0.24***	-0.05ns	0.36***	0.26***	-0.30***	0.08ns	-0.30***	-0.10ns
	$dT_{\min}$	0.35***	0.24***	-0.06ns	0.31***	0.38***	0.06ns	-0.06ns	-0.23***	0.21***	-0.13**	0.39***
w1c1	$dT_{\max}$	0.10***	0.25***	-0.07**	0.22***	-0.02ns	0.30***	0.10***	-0.25***	-0.01ns	-0.20***	-0.09***
	$dT_{\min}$	0.20***	0.09***	0.05ns	0.15***	0.27***	-0.05ns	-0.06	-0.08	0.18	0.02ns	0.37***
w2c2	$dT_{\max}$	0.16**	0.30***	-0.09ns	0.28***	0.06ns	0.32***	0.08ns	-0.30***	-0.01ns	-0.21***	-0.12*
	$dT_{\min}$	0.12*	0.10ns	0.03ns	0.12**	0.16	0.02ns	0.02ns	-0.10ns	0.10ns	-0.06ns	0.07ns
w0c2	$dT_{\max}$	0.04ns	0.10ns	-0.03ns	0.08ns	-0.01ns	0.11ns	0.13ns	-0.10ns	-0.01ns	-0.18**	-0.07ns
	$dT_{\min}$	0.17**	0.17**	-0.15*	0.17**	0.19**	0.09ns	-0.01ns	-0.16**	0.09ns	-0.13ns	0.24***
w2c0	$dT_{\max}$	0.12***	0.27***	-0.01ns	0.25***	0.03ns	0.29***	0.10***	-0.27***	0.11***	-0.23***	-0.06*
	$dT_{\min}$	0.27***	0.25***	0.05ns	0.30***	0.34	0.08*	0.05ns	-0.24***	0.20***	-0.14***	0.17***

The gradients represent the degree of correlations whereas the colours denote positive (pink) and negative (blue) correlations. \*\*\* $p < 0.01$ , \*\* $p < 0.05$ , \* $p < 0.1$ , ns:  $p \geq 0.1$ .

temperature ( $dT_{\max}$ ) from the reference site during the summer is shown below (Equation (7)).

$$dT_{\max} = c_0 + c_{\text{MD}} \cdot \text{MD} + c_{\text{BS}} \cdot f_{\text{BS}} + c_{\text{TV}} \cdot f_{\text{TV}} + c_{\text{vol}} \cdot h_{\text{B}} \cdot f_{\text{BS}} + c_z \cdot z + \varepsilon \quad (7)$$

The intercept  $c_0$  is 0.28 K, the values of the regression coefficients  $c_{\text{MD}}$ ,  $c_{\text{BS}}$ ,  $c_{\text{TV}}$ ,  $c_{\text{vol}}$ , and  $c_z$  are 1.18, 0.5 K, -0.8 K, -0.05 K m<sup>-1</sup>, and -0.002 K m<sup>-1</sup>, respectively.  $\varepsilon$  is an error term for the regression analysis. The explained variance  $R^2$  is 0.42 ( $N = 320$ ). The regression coefficients are significant at the  $p = 0.20$  level.

Table 4. Correlation coefficients between the CAS output variables and the temperature deviations ( $dT_{\max}$  and  $dT_{\min}$ ) from the reference station (Seoul weather station) at the 50 sites in the SR for the four seasons.

Class	Temperature	$dT_{\text{SHF}}$	$dT_{\text{ca}}$	MD	TD	$f_{\text{BS}}$	$f_{\text{US}}$	$f_{\text{ws}}$	$f_{\text{vs}}$	$f_{\text{TV}}$	$h_B$	$h_V$	$z$
	Spring												
w0c0	$dT_{\max}$	0.29***	0.37***	0.56***	0.47***	0.27***	0.06*	0.05ns	-0.18***	-0.18***	0.14***	-0.01ns	-0.55***
	$dT_{\min}$	0.14***	0.13***	0.09***	0.17***	0.09**	0.07**	0.14***	-0.02ns	-0.17***	0.15***	-0.13***	-0.01ns
w1c1	$dT_{\max}$	0.25***	0.34***	0.55***	0.43***	0.22***	0.05***	0.05***	-0.14***	-0.17***	0.12***	-0.05**	-0.55***
	$dT_{\min}$	0.25***	0.26***	0.30***	0.35***	0.20***	0.11***	0.14***	-0.09***	-0.25***	0.19***	-0.11***	-0.26***
w2c2	$dT_{\max}$	0.24***	0.33***	0.50***	0.41***	0.21***	0.08***	0.06**	-0.09***	-0.23***	0.13***	-0.07***	-0.55***
	$dT_{\min}$	0.34***	0.40***	0.54***	0.52***	0.30***	0.14***	0.09***	-0.11***	-0.35***	0.21***	-0.12***	-0.62***
w0c2	$dT_{\max}$	0.30***	0.36***	0.57***	0.50***	0.28***	0.08***	0.05**	-0.11***	-0.27***	0.16***	-0.09***	-0.61***
	$dT_{\min}$	0.32***	0.32***	0.42***	0.45***	0.27***	0.12***	0.11***	-0.12***	-0.30***	0.22***	-0.14***	-0.42***
w2c0	$dT_{\max}$	0.19***	0.31***	0.61***	0.41***	0.17***	0.05***	0.04**	-0.10***	-0.14***	0.08***	-0.05**	-0.63***
	$dT_{\min}$	0.29***	0.30***	0.36***	0.41***	0.24***	0.12***	0.12***	-0.09***	-0.30***	0.19***	-0.10***	-0.37***
	Summer												
w0c0	$dT_{\max}$	0.30***	0.34***	0.61***	0.50***	0.28***	0.10*	0.03ns	-0.14**	-0.24***	0.09*	-0.05 ns	-0.59***
	$dT_{\min}$	0.31***	0.32***	0.31***	0.42***	0.26***	0.16***	0.08ns	-0.02ns	-0.39***	0.18***	-0.26***	-0.31***
w1c1	$dT_{\max}$	0.28***	0.32***	0.58***	0.47***	0.27***	0.08***	0.06***	-0.14***	-0.23***	0.10***	-0.10***	-0.58***
	$dT_{\min}$	0.32***	0.29***	0.39***	0.45***	0.26***	0.13***	0.15***	-0.10***	-0.33***	0.20***	-0.21***	-0.37***
w2c2	$dT_{\max}$	0.27***	0.31***	0.56***	0.47***	0.25***	0.11***	0.09***	-0.10***	-0.28***	0.12***	-0.11***	-0.63***
	$dT_{\min}$	0.32***	0.33***	0.55***	0.51***	0.27***	0.14***	0.12***	-0.10***	-0.34***	0.18***	-0.12***	-0.62***
w0c2	$dT_{\max}$	0.29***	0.33***	0.53***	0.47***	0.27***	0.10***	0.07***	-0.10***	-0.30***	0.10***	-0.11***	-0.60***
	$dT_{\min}$	0.30***	0.29***	0.44***	0.45***	0.26***	0.09***	0.10***	-0.08***	-0.32***	0.16***	-0.17***	-0.47***
w2c0	$dT_{\max}$	0.23***	0.30***	0.57***	0.43***	0.20***	0.10**	0.01ns	-0.09*	-0.20***	0.06ns	-0.06ns	-0.60***
	$dT_{\min}$	0.28***	0.31***	0.35***	0.40***	0.22***	0.14***	0.15***	-0.04ns	-0.35***	0.19***	-0.11**	-0.36***
	Autumn												
w0c0	$dT_{\max}$	0.27***	0.34***	0.62***	0.47***	0.25***	0.06**	0.05*	-0.15***	-0.18***	0.11***	0.01ns	-0.66***
	$dT_{\min}$	0.09***	0.08**	0.05*	0.12***	0.05*	0.06**	0.19***	-0.00ns	-0.16***	0.09***	-0.11***	0.01ns
w1c1	$dT_{\max}$	0.24***	0.33***	0.58***	0.45***	0.22***	0.05***	0.07***	-0.10***	-0.22***	0.09***	-0.05***	-0.65***
	$dT_{\min}$	0.17***	0.16***	0.21***	0.25***	0.13***	0.09***	0.17***	-0.05***	-0.21***	0.12***	-0.12***	-0.17***
w2c2	$dT_{\max}$	0.23***	0.32***	0.56***	0.46***	0.22***	0.10***	0.09***	-0.10***	-0.25***	0.13***	-0.06***	-0.67***
	$dT_{\min}$	0.25***	0.31***	0.45***	0.41***	0.21***	0.13***	0.14***	-0.09***	-0.28***	0.13***	-0.07***	-0.49***
w0c2	$dT_{\max}$	0.24***	0.34***	0.54***	0.43***	0.22***	0.09***	0.09***	-0.09***	-0.25***	0.09***	-0.06***	-0.62***
	$dT_{\min}$	0.24***	0.28***	0.39***	0.39***	0.19***	0.14***	0.16***	-0.05**	-0.31***	0.13***	-0.15***	-0.42***
w2c0	$dT_{\max}$	0.21***	0.31***	0.64***	0.45***	0.18***	0.07***	0.05**	-0.05**	-0.22***	0.08***	-0.04*	-0.72***
	$dT_{\min}$	0.25***	0.28***	0.34***	0.37***	0.21***	0.14***	0.13***	-0.03ns	-0.33***	0.15***	-0.11***	-0.37***
	Winter												
w0c0	$dT_{\max}$	0.29***	0.40***	0.63***	0.50***	0.27***	0.07***	0.02ns	-0.11***	-0.25***	0.15***	0.01ns	-0.69***
	$dT_{\min}$	0.13***	0.16***	0.12***	0.17***	0.08***	0.06**	0.11***	-0.01ns	-0.17***	0.11***	-0.08***	0.07***
w1c1	$dT_{\max}$	0.24***	0.37***	0.58***	0.45***	0.22***	0.07***	0.03**	-0.08***	-0.23***	0.12***	-0.04***	-0.66***
	$dT_{\min}$	0.22***	0.22***	0.25***	0.30***	0.17***	0.09***	0.10***	-0.07***	-0.22***	0.14***	-0.09***	-0.21***
w2c2	$dT_{\max}$	0.28***	0.33***	0.55***	0.47***	0.25***	0.08**	0.04ns	-0.09***	-0.26***	0.15***	-0.07**	-0.63***
	$dT_{\min}$	0.27***	0.32***	0.43***	0.42***	0.23***	0.14***	0.07**	-0.09***	-0.27***	0.15***	-0.09***	-0.48***
w0c2	$dT_{\max}$	0.22***	0.35***	0.48***	0.39***	0.19***	0.08**	0.04ns	-0.07*	-0.21***	0.15***	0.02ns	-0.54***
	$dT_{\min}$	0.19***	0.20***	0.22***	0.24***	0.13***	0.07**	0.09**	-0.07*	-0.15***	0.16***	-0.03ns	-0.16***
w2c0	$dT_{\max}$	0.26***	0.40***	0.63***	0.50***	0.24***	0.08***	0.02ns	-0.03*	-0.32***	0.11***	-0.07***	-0.74***
	$dT_{\min}$	0.26***	0.35***	0.41***	0.42***	0.23***	0.13***	0.07***	-0.03**	-0.34***	0.14***	-0.09***	-0.48***

The gradients represent the degree of correlation whereas the colours denote the sign. \*\*\* $p < 0.01$ , \*\* $p < 0.05$ , \* $p < 0.1$ , ns:  $p \geq 0.1$ .

In Equation (7), the estimated  $dT_{\max}$  is the temperature difference during the summer days between the site of interest and the reference SWS. Each coefficient in the equation is an impact parameter for each variable. The intercept level reveals that the SWS is about 0.3 K cooler than the other stations in Seoul on average. The

large open space, in which the SWS is located, induces this cooling effect even during the daytime. The regression coefficients of  $f_{\text{BS}}$  and  $f_{\text{TV}}$  indicate that the impact of the  $f_{\text{TV}}$  on  $dT_{\max}$  was greater than that of  $f_{\text{BS}}$  by 60% (-0.8 vs 0.5 K). The areal fraction maps (Figures 3 and 4) show that TV is more sparsely distributed inside the urban

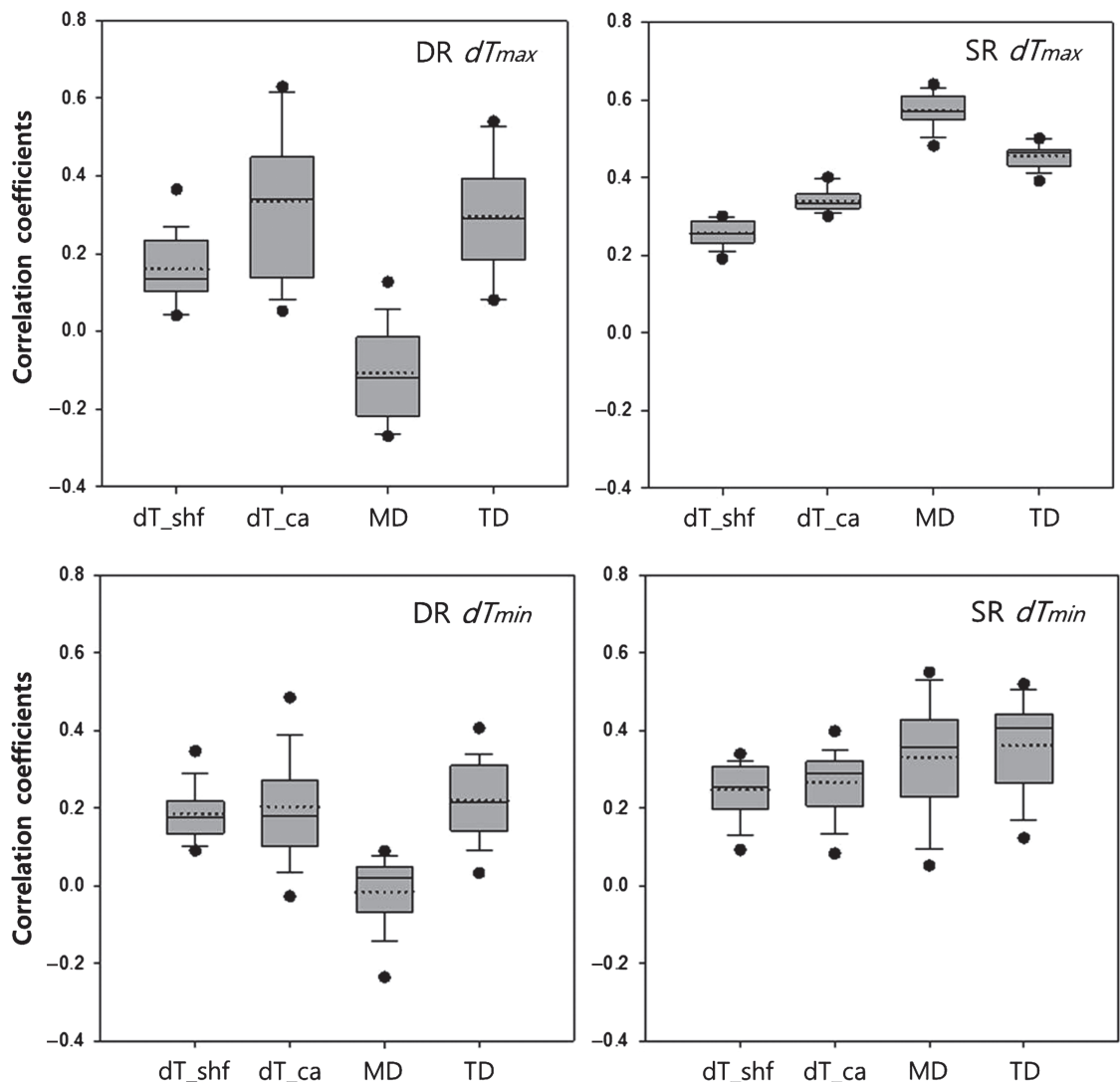


Figure 8. Correlation coefficients between daily maximum/minimum temperature deviation ( $dT_{\max}/dT_{\min}$ ) and the CAS output variables ( $dT_{\text{SHF}}$ ,  $dT_{\text{ca}}$ , MD, and TD) in domains DR and SR. Median and mean values of the coefficient values are indicated as solid and dashed lines.

areas than BS so that the meso-scale analysis (MD) did not efficiently resolve the cooling effect of the TV. This resulted in the larger unresolved temperature impact of  $f_{\text{TV}}$  than of  $f_{\text{BS}}$  after the meso-scale analysis. The  $h_B \cdot f_{\text{BS}}$  term is equivalent to the building volume, and it indicates that taller buildings with the same footprint will reduce the temperature by 0.05 K per 1 m of building height. This negative impact is reasonable because shadows by the buildings will increase with higher building volumes. However, the impact by the building volumes was minor when compared to that by the  $f_{\text{BS}}$  or  $h_B$  alone.

The correlation analysis in the DR showed a negative correlation of the MD to the deviation of the maximum temperature ( $dT_{\max}$ ) in summer. However, the correlation coefficient in the SR was positive and the MD variable was included in the TD' model. The regression coefficient of MD ( $c_{\text{MD}} = 1.18$ ) reveals the meso-scale model underestimated the temperature deviation over SR by 18%.

### 3.2.2. Mapping and evaluation of the detailed temperature distribution – TD'

**3.2.2.1. Development of a detailed map of temperature distribution based on the TD' model:** The temperature distribution (TD') in the SR was calculated using the TD' model based on the 25 m resolution land cover data (Figure 9). It represents the temperature distribution when the temperature at the SWS is 33 °C, which is the standard threshold temperature for heat advisory in Korea. Most of the built-up areas in Seoul are exposed to at least this threshold temperature. However, it is not easy to assess the heat stress and make spatial plans to avoid the stress at this resolution.

The same TD' model was applied to the DR region at a higher resolution of 5 m (Figure 10). The footage of individual buildings is distinguishable by the angular shape, size, and layout and by the lower roof temperature than the surface temperature in the output. This shows that most of the DR area has lower temperature than the other parts of the city. The lower temperature could have been

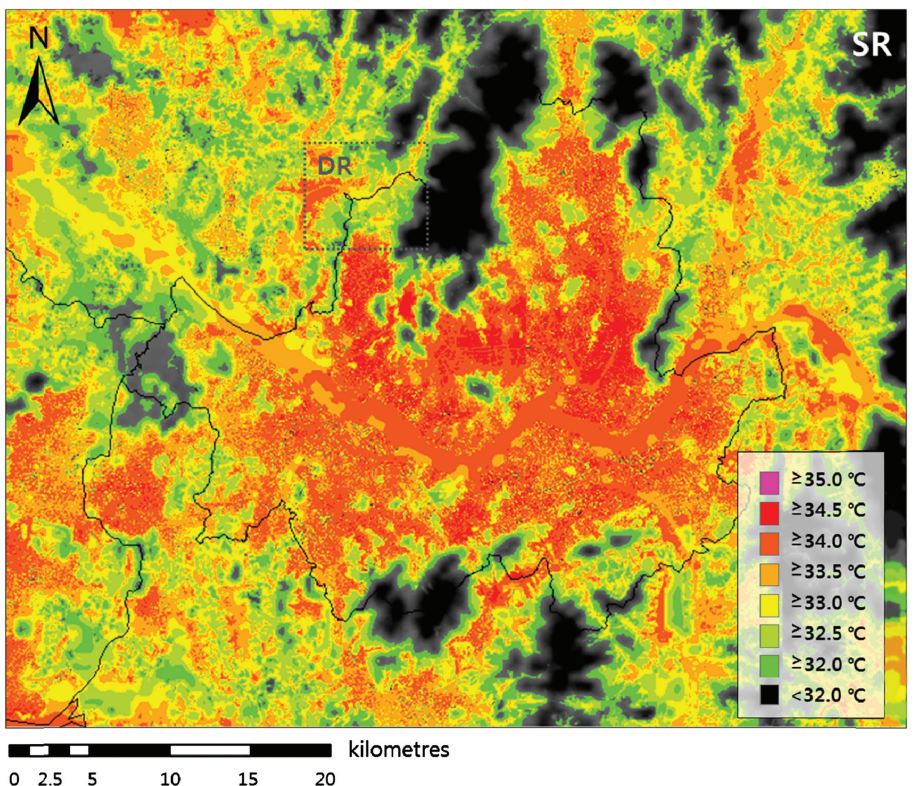


Figure 9. Maximum temperature distribution map of the SR based on the TD' model and an observed daily maximum temperature of  $33^{\circ}\text{C}$  at the Seoul weather station (the threshold temperature for heat advisory in Korea).

brought on by (1) the lower areal building density inside the DR, and (2) the cold air production from the nearby mountains.

**3.2.2.2. Evaluation of the TD' model based on observations:** In Figure 11, only the temperatures from the eight common observational sites in 2007 and 2011 (P1, P2, P4–P9) were compared. Because the input data assimilated in CAS represented the surface conditions of 2011, the regression analysis between the predicted and observed maximum temperature showed a better relationship in 2011 than in 2007. The coefficient of determination was higher and the slope was closer to 1.0 in 2011 than in 2007.

The current TD' model, which was developed based on the analysis of CAS and observed temperature deviations in the SR, was able to estimate the daily maximum temperature using the detailed information from CAS for 2011 in the DR. However, during the model development, it did not have the land cover and surface elevation at the highest possible resolution in the SR. This could have led to the systematic errors of site dependency in Figure 11(b) – individual regression model of the eight ‘P’ sites had different slope (regression models are not shown here). The TD' model can be further improved by refining the input data of the SR in CAS. However, it should also be considered that the air temperatures are spatially not that variable and there are other possible sources of errors on the observation and the model itself.

#### 4. Conclusions

CAS was developed based on the concept of integrating a meso-scale model and a sub-scale analysis. It was evaluated using the observed temperature at two different scales in and around Seoul. The correlation analyses at different scales revealed the differences of the observational scales. The differences between the observed and predicted temperature deviations at different scales match the original concept of CAS. The detailed temperature deviation from the high density observation was correlated with the high-resolution analysis results such as the local-scale air temperature deviation (LD) in the DR, whereas the meso-scale analysis results were significant in the coarse SR. It is concluded that the multi-scale approach followed by the CAS workbench is generally suitable. This is particularly revealed by the fact that the meso-scale air temperature deviation (MD) works well in the SR, where meso-scale processes are non-negligible, but not very good in the DR, where local-scale processes are dominant. The results also indicate that there is room for further improvements. An urban canopy type model would provide an improved basis for the meso-scale contribution to the local heating especially in areas characterized by high building density and prevalence of tall buildings, and complex street canyons.

The SWS was selected as the reference for the temperature deviation so that the model can estimate actual temperature distribution. By incorporating a reference station in the study area, the CAS workbench can now

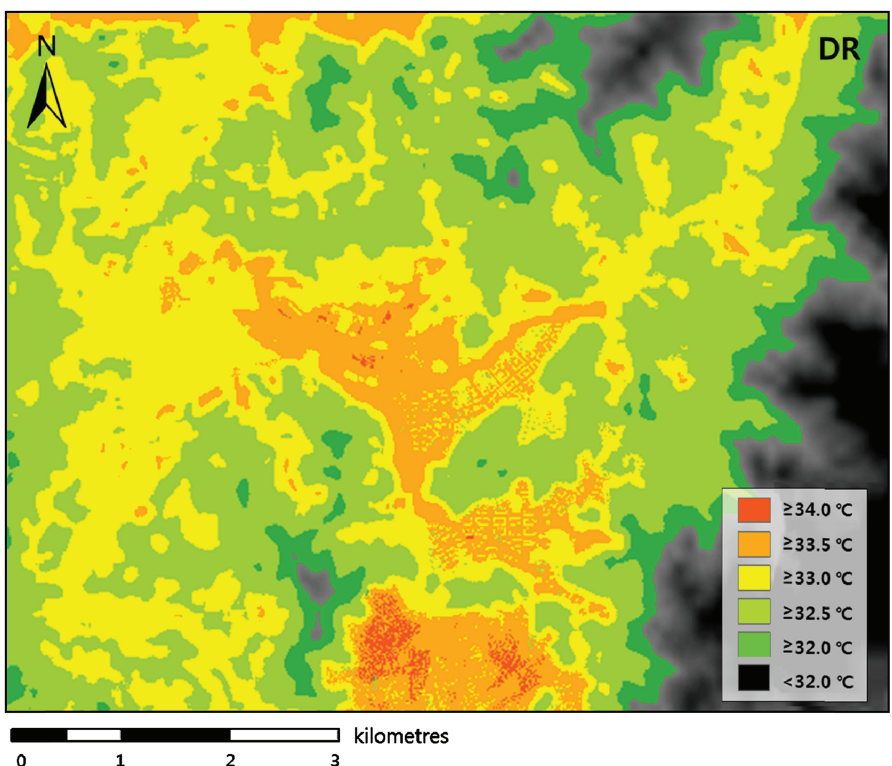


Figure 10. Maximum temperature distribution map of the DR based on the TD' model and an observed daily maximum temperature of 33 °C at the Seoul weather station (the threshold temperature for heat advisory in Korea).

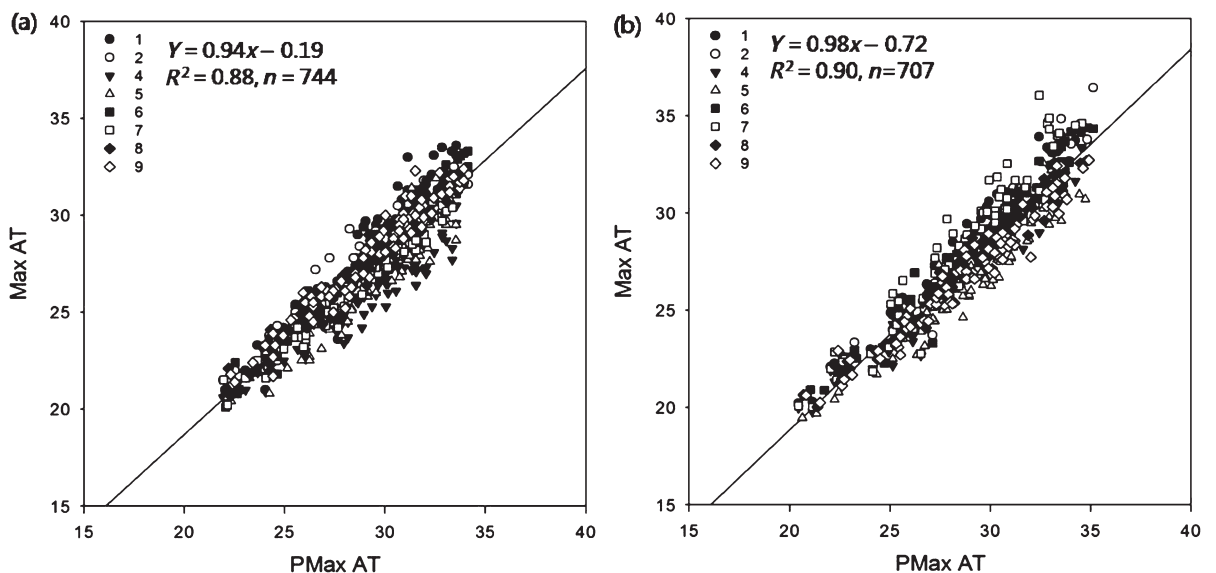


Figure 11. Observed (MaxAT) and predicted (PMaxAT) daily maximum temperature at the 8 sites (P1, P2, P4–P9) in the DR during the summers of (a) before (2007) and (b) after (2011) the new-town development.

estimate the actual temperature distribution and can be used in comparison studies for various scenarios such as urban developmental planning and urban climate change scenarios. It is necessary to implement a better definition of initial and boundary conditions for the meso-scale model for idealized simulations, or to switch to real case simulations, which means that MetPhoMod needs to be substituted by another model because it does not account for cloud-radiation feedbacks.

The maximum temperature distribution maps (Figures 9 and 10) show the importance of the positioning and density of buildings and vegetation in city planning to prevent or reduce the heat stress during the summer months. The integrated CAS – TD' model can be utilized to assess actual heat wave events in the past and future so that any areas with higher vulnerability to heat waves can be detected and considered in re-development plans. It is now possible to compare two periods by using the

same reference station between the periods. Through the analysis of high density observation and comparison, it can be concluded that optimized analysis with detailed information is necessary for the assessment of thermal impact in small areas using high density observation. The methodology utilized in this study can be transferred to other cities having different urban structures. As a next step, we will transfer this approach to other Korean cities.

## Acknowledgements

This work was funded by the Korea Meteorological Administration Research and Development Program under Grant Weather Information Service Engine (WISE) project, KMA-2012-0001. The authors appreciate the anonymous reviewers for their comments and suggestions in improving the manuscript.

## References

- Baik J-J, Park S-B, Kim J-J. 2009. Urban flow and dispersion simulation using a CFD Model coupled to a mesoscale model. *J. Appl. Meteorol. Climatol.* **48**: 1667–1681.
- Bhang KJ, Park S-S. 2009. Evaluation of the surface temperature variation with surface settings on the urban heat island in Seoul, South Korea using Landsat-7 ETM+ and SPOT. *IEEE Geosci. Remote Sens. Lett.* **6**(4): 708–712.
- Chow W, Roth M. 2006. Temporal dynamics of the urban heat island of Singapore. *Int. J. Climatol.* **26**: 2243–2260.
- Chow WT, Pope RL, Martin CA, Brazel AJ. 2011. Observing and modeling the nocturnal park cool island of an arid city: horizontal and vertical impacts. *Theor. Appl. Climatol.* **103**(1–2): 197–211.
- Christen A, Vogt R. 2004. Energy and radiation balance of a Central European City. *Int. J. Climatol.* **24**: 1395–1421.
- Chung U, Seo HH, Hwang KH, Hwang BS, Choi J, Lee JT, Yun JI. 2006. Minimum temperature mapping over complex terrain by estimating cold air accumulation potential. *J. Agric. For. Meteorol.* **137**: 15–24.
- Chung U, Jung J-E, Seo H-C, Yun JI. 2009. Using urban effect corrected temperature data and a tree phenology model to project geographical shift of cherry flowering date in South Korea. *J. Clim. Change* **93**: 447–463, doi: 10.1007/s10584-008-9504-z.
- Cui Z, Cai X, Baker CJ. 2004. Large-eddy simulation of turbulent flow in a street canyon. *Q. J. R. Meteorol. Soc.* **130**: 1373–1394.
- Eum JH. 2008. *Integration of Climate Information into Spatial Planning in Seoul, South Korea*, PhD dissertation, Technical University of Berlin, Berlin.
- Grimmond CSB, Roth M, Oke TR, Au YC, Best M, Betts R, Carmichael G, Cleugh H, Dabberdt W, Emmanuel R, Freitas E, Fortuniak K, Hanna S, Klein P, Kalkstein LS, Liu CH, Nickson A, Pearlmuter D, Sailor D, Voogt J. 2010. Climate and more sustainable cities: climate information for improved planning and management of cities (producers/capabilities perspective). *Environ. Sci.* **1**: 247–274.
- Kim Y-H, Baik J-J. 2005. Spatial and temporal structure of the urban heat island in Seoul. *J. Appl. Meteorol. Climatol.* **44**: 591–605, doi: 10.1175/JAM2226.1.
- Kim KR, Yi C, Scherer D, Jung H-S. 2013. Impact of distance from the city-core and land cover on air temperature in Seoul metropolitan area (in Korean). In *Proceedings of the Spring Meeting of the Korea Meteorology Society*, Seoul, 496–497.
- Kim KR, Yi C, Lee J-S, Meier F, Jaenicke B, Fehrenbach U, Scherer D. 2014. BioCAS: Biometeorological Climate impact Assessment System for building-scale impact assessment of heat-stress related mortality. *Die Erde* **145**: 62–79.
- Lengfeld K, Ament F. 2012. Observing local-scale variability of near-surface temperature and humidity using a wireless sensor network. *J. Appl. Meteorol. Climatol.* **51**: 30–41, doi: 10.1175/JAMC-D-11-025.1.
- Mosimann T, Frey T, Trute P. 1999. Schutzgut Klima/Luft in der Landschaftsplanung. *Inf.dienst Nat.schutz Niedersachs.* **19**(4): 201–276.
- NIMR. 2009. *Understanding Climate Change III – The Climate Change of Seoul*. National Institute of Meteorological Research, Seoul, 67 pp.
- Oke TR. 1982. The energetic basis of the urban heat island. *Q. J. R. Meteorol. Soc.* **108**: 1–24.
- Oke TR. 1987. *Boundary Layer Climates*, 2nd edn. Routledge: London and New York, NY.
- Parlow E, Scherer D, Fehrenbach U. 2006. *Regionale Klimaanalyse der Region Südlicher Oberrhein (REKLISO)*. Regionalverband Südlicher Oberrhein. Abschlussbericht. 99 S. <http://www.rvso.de> (accessed 31 March 2015).
- Parlow E, Scherer D, Fehrenbach U. 2010. *Klimaanalyse der Stadt Zürich (KLAZ)*. Umwelt- und Gesundheitsschutz der Stadt Zürich. Abschlussbericht. 76 S. <http://www.stadt-zuerich.ch> (accessed 31 March 2015).
- Perego S. 1999. Metphomod – a numerical mesoscale model for the simulation of regional photosmog in complex terrain: model description and application during Pollumet 1993 (Switzerland). *Meteorol. Atmos. Phys.* **70**: 43–69.
- Roth M. 2007. Review of urban climate research in (sub)tropical regions. *Int. J. Climatol.* **27**: 1859–1873.
- Ryu YH, Baik JJ. 2012. Daytime local circulations and their interactions in the Seoul metropolitan area. *J. Appl. Meteorol. Climatol.* **52**: 784–801.
- Ryu YH, Baik JJ, Lee SH. 2011. A new single-layer urban canopy model for use in mesoscale atmospheric models. *J. Appl. Meteorol. Climatol.* **50**: 1773–1794.
- Schaer C, Jendritzky G. 2004. Hot news from summer 2003 – the European heatwave 2003. *Nature* **432**: 559–560.
- Scherer D, Fehrenbach U, Beha H-D, Parlow E. 1999. Improved concepts and methods in analysis and evaluation of the urban climate for optimizing urban planning processes. *Atmos. Environ.* **33**: 4185–4193.
- Seo H-C, Jeon S-J, Yun JI. 2008. Azimuthal distribution of daily maximum temperatures observed at sideslopes of a grass-covered inactive parasitic volcano (“Ohreum”) in Jeju Island. *Korean J. Agric. For. Meteorol.* **10**(1): 25–31 (in Korean with English abstract).
- SMG. 2009. Seoul Metropolitan Government Ordinance No. 4883 on Environmental Impact Assessment. <http://legal.seoul.go.kr/legal/english/front/page/law.html?pAct=lawView&pPromNo=406> (accessed 31 March 2015).
- Stott PA, Stone DA, Allen MR. 2004. Human contribution to the European heatwave of 2003. *Nature* **432**: 610–613.
- UBIN. 2010. Urban Information Network. Population Statistics of World Urban. <http://ubin.krihs.re.kr> (original source: <http://www.un.org>) (accessed 31 March 2015).
- Yi C, Choi Y-J, Eum J-H, Kim G-H, Kim KR, Scherer D, Fehrenbach U. 2010. Development of climate analysis software for urban and environmental of Seoul. In *Proceedings of the 7th Conference on Biometeorology*, Freiburg, Germany, 455–460.
- Yi C, Eum J-H, Choi Y-J, Kim KR, Scherer D, Fehrenbach U, Kim G-H. 2011a. Development of Climate Analysis Seoul (CAS) maps based on landuse and meteorological model. *J. Korean Assoc. Geogr. Inf. Stud.* **14**(1): 12–25 (in Korean with English Abstract).
- Yi C, Kim KR, Choi Y-J, An SM, Scherer D, Fehrenbach U. 2011b. Improvement of Climate Analysis Seoul (CAS) based on high resolution LiDAR data and meteorological model. In *EMS Annual Meeting Abstracts*, Berlin, 12–16 September, Vol. 8. EMS2011-825.
- Yi C, An SM, Kim KR, Choi Y-J, Scherer D. 2012a. Improvement of air temperature analysis by precise spatial data on a local-scale – a case study of Eunpyeong New-town in Seoul. *J. Korean Assoc. Geogr. Inf. Stud.* **15**(1): 144–158 (in Korean with English abstract).
- Yi C, Kim KR, Choi Y-J, Park YS, Kwon TK, Kim G-H, Won HY, Lee SY, Kim MS, Choi JM, Scherer D. 2012b. CAS: evaluation of fine scale temperature and wind analysis. In *Proceedings of the 8th International Conference on Urban Climate and 10th Symposium on the Urban Environment*, Dublin, 179 pp.
- Yi C, Kim KR, An SM, Choi YJ. 2014. Impact of the local surface characteristics and the distance from the center of heat island to suburban areas on the night temperature distribution over the Seoul metropolitan area. *J. Korean Assoc. Geogr. Inf. Stud.* **17**(1): 35–49.
- Yu C, Hien WN. 2006. Thermal benefits of city parks. *Energy Build.* **38**(2): 105–120.
- Yun JI. 2007. Applications of "high definition digital climate maps" in restructuring of Korean agriculture. *Korean J. Agric. For. Meteorol.* **9**(1): 1–16 (in Korean with English Abstract).
- Yun JI. 2010. Agroclimatic maps augmented by a GIS technology. *Korean J. Agric. For. Meteorol.* **12**(1): 63–73 (in Korean with English Abstract).